JOURNAL OF GEOPHYSICAL RESEARCH, VOL. 104, NO. A1, PAGES 247-261, JANUARY 1, 1999

Magnetopause shape determinations from measured position and estimated flaring angle

H. Kawano,[1,2] S. M. Petrinec,[3] C. T. Russell,[4] and T. Higuchi[5]

Abstract. In this paper we unify two approaches to determining magnetopause shape and location from observations by fitting one model simultaneously to both the crossing data and the calculated data of magnetopause flaring angle, to achieve more accurate magnetopause shapes. We prepare two magnetopause models, each of which is an ellipsoid from the subsolar point to the position where the distance of the ellipsoid from the X axis is maximum. The model magnetopause beyond this position is a cylinder attached to the edge of the ellipsoid at this location. This choice of shapes makes it easier to compare our results with earlier work which fit ellipsoids to (only) crossing data. In one of our two models, the focus of the ellipsoid lies at the center of the Earth, whereas in the other it lies at a position determined from fits to the data. We use a statistical criterion (called AIC) that lets us objectively determine which model better fits the data. As a result, we find that a model with an off-center focus better expresses the nature of the observed data. Despite differing mathematical formulations, our model results generally resemble those of *Petrinec and Russell* [1996]. Consequently, the mathematical expression is not the major reason why these models flare more (less) than the model of *Roelof and Sibeck* [1993] for very small (large) solar wind dynamic pressure.

1. Introduction

In magnetospheric physics it is important to have a concise model for the shape of the magnetopause, because when one studies magnetospheric or magnetosheath phenomena observed in situ one often needs an estimate of the magnetopause location. Magnetopause models can also help us understand the nature of the solar wind-magnetosphere interaction. Thus several recent papers have presented models for the shape of the magnetopause. Most of these models have adopted an ellipsoidal magnetopause [e.g., *Petrinec et al.*, 1991; *Roelof and Sibeck*, 1993] and fit this model to subsets of observed magnetopause crossings. However, the input data sets consist principally of dayside magnetopause crossings, owing to the orbital coverage of the satellites used. As a result, it is not clear to what downtail distance the models are valid.

To increase the number of postterminator data usable for the model fitting, *Petrinec and Russell* [1996] (referred to as PR96 below) employed a method using the lobe magnetic field data, first used by *Fairfield* [1985] in a case study and by *Nakai et al.* [1991] in a statistical study. That is, by using the lobe field data observed by the ISEE 2 spacecraft and the simultaneous solar wind pressure data from IMP 8, PR96 calculated the magnetopause flaring angle, α, which was defined as the angle between the solar wind flow direction and the tangent to the magnetopause, by assuming that (1) the lobe magnetic field is uniform from the satellite position to the tail magnetopause, that (2) the lobe magnetic pressure balances the solar wind pressure impinging onto the magnetopause, and that (3) the solar wind pressure is approximated by the sum of solar wind dynamic pressure, thermal pressure, and magnetic pressure.

Because lobe field observations were made continuously for each ISEE 2 pass through the magnetotail, PR96 were able to substantially increase the amount of data in the range $0\ R_E \geq X \geq -22\ R_E$ (in the aberrated GSM coordinate system). They used the data to determine the magnetopause shape: By modeling the X dependence of α and by integrating the modeled α down the magnetotail, PR96 obtained the radius of the postterminator magnetopause as a function of X. As the initial value of integration at the terminator ($X = 0$), they used the distance at the terminator of the model magnetopause of *Petrinec et al.* [1991] and *Petrinec and Russell* [1993], determined from a geocentric ellipsoid fit to ISEE 1 and 2 magnetopause crossings (mainly dayside). The functional form of the postterminator magnetopause was empirically determined from the distribution of α, and its radius had an X dependence in the form of

$$C_1 \arcsin(e^{C_2 X + C_3}) + C_4 , \quad (1)$$

[1]Solar-Terrestrial Environment Laboratory, Nagoya University, Toyokawa, Aichi, Japan.

[2]Now at Department of Earth and Planetary Sciences, Kyushu University, Hakozaki, Fukuoka, Japan.

[3]Lockheed Martin Advance Technology Center, Palo Alto, CA.

[4]Institute of Geophysics and Planetary Physics, University of California, Los Angeles.

[5]Institute of Statistical Mathematics, Minami-Azabu, Tokyo, Japan.

Paper number 98JA02479.
0148-0227/99/98JA-02479$09.00

where C_1, C_2, C_3, and C_4, are constants (for a given solar wind condition). This tail radius approaches an asymptotic value for $X \rightarrow -\infty$ because C_2 is always positive in their model. On the other hand, the same functional form cannot be used for the dayside, because it causes a discrete jump in the normal direction at the subsolar point.

We note that *Sibeck et al.* [1986] used empirical models of the lobe field strength and nominal values of the solar wind parameters to obtain nominal magnetopause flaring angle profiles as a function of X, and then calculated tail magnetopause shapes by integrating the obtained flaring angle profiles with X.

Compared with the model of *Roelof and Sibeck* [1993] (referred to as RS93 below), who fit a geoeccentric ellipsoid to the largest data set of the magnetopause crossings in the literature, the PR96 model agreed very well in the range $0\ R_E > X > -30\ R_E$ for a nominal value of the solar wind pressure. On the other hand, when the solar wind pressure values were much smaller (larger) than the nominal value, the PR96 model flared much more (less) than the RS93 model. However, the difference may partly come from the quite different mathematical forms of the two models.

The purpose of this paper is to incorporate both the position data of *Petrinec and Russell* [1991] and the α data of PR96 in the ellipsoidal model, and to compare the results with other models. Since the ellipsoid is usable from the subsolar point to the point of the maximum tail radius, there is no need to connect two models at $X = 0$ like PR96 did, which causes a discontinuous shape (a bump or a dip) of the magnetopause at $X = 0$. In the region tailward of the maximum radius point, we will just use a cylinder with a constant tail radius given by the maximum tail radius of the ellipsoid. We do this in order to avoid a downtail decrease of the tail radius. There is no bump or dip in the magnetopause shape where the two parts are connected, that is, at X where the tail radius of the ellipsoid reaches maximum. By fitting the "dayside" magnetopause crossing data of *Petrinec et al.* [1991] along with the α data, we increase the reliability of the fit model.

We also address the problem of how meaningful it is to move the focus of the ellipsoid away from the center of the Earth. If one fixes the focus of the ellipsoid at the center of the Earth, one has two model parameters, the ellipticity, ε, and the minimum radius from the focus, r_0. For example, *Holzer and Slavin* [1978] and *Petrinec et al.* [1991] used such a model. On the other hand, for example *Slavin et al.* [1983] and *Roelof and Sibeck* [1993] also used the focal point of the ellipsoid, x_0, as a third parameter to fit. However, the addition of x_0 was made without testing whether the new parameter was necessary. In general if one fits models to a data set, it is a matter of course that the mean square residual of the data from the model decreases with an increasing number of model parameters. However, this does not mean that the addition of a new parameter always improves the model: The addition tends to decrease the precision/reliability of already existing fit parameters. For example in our case, the addition of x_0 tends to decrease the precision/reliability of fit ε and r_0, as we will show later (in Figures 3 and 5). In this paper we present an objective approach to judge whether the 3-parameter model fits a data set better or worse than the 2-parameter model.

2. Data

The magnetopause crossing data set used in this paper is the same as that used by *Petrinec et al.* [1991]. The data set of α is the same as that used by PR96. Both data sets are associated with 5-min averaged data of solar wind dynamic pressure, $P_{SW,\mathrm{dyn}} = \rho v_{SW}^2$, where ρ and v_{SW} are the ion mass density and the bulk speed of the solar wind, and B_Z, in GSM coordinates, of the interplanetary magnetic field (IMF). The position of the satellite is expressed in the aberrated GSM coordinate system, in which the X axis is aberrated by $\sim 4°$ to account for the average deflection of the solar wind from the Sun-Earth line. More details on the data sets can be found in the above papers.

Only data when the IMF was northward are used in this paper to study the $P_{SW,\mathrm{dyn}}$ dependence of the magnetopause shape, and no distinction is made between any two data associated with the same $P_{SW,\mathrm{dyn}}$ and different IMF values. We apply this restriction in order to simplify this paper and concentrate on the two major points of this paper, as described in last two paragraphs of section 1. We note that *Petrinec and Russell* [1993] have suggested that the (dayside) magnetopause shape is not affected much by the IMF when it is northward. If that is the case, the magnetopause shape obtained below is not just an averaged shape but an actual shape common to wide variety of the IMF $B_z > 0$. However, we also note that *Sibeck et al.* [1991] and RS93 have suggested that the subsolar magnetopause moves outward for increasing IMF $B_z > 0$. If that is the case, the magnetopause shape obtained below is the average shape which would be close to the shape under the data-averaged value of the northward IMF B_z.

The solar wind thermal pressure, $P_{SW,th}$, is not treated as a control parameter for the magnetopause shape in this paper (although $P_{SW,th}$ is taken into account when we calculate α from each data point, as stated below). Most previous models (e.g., RS93; PR96) did the same. $P_{SW,th}$ should scarcely affect the dayside shape of the magnetopause, because $P_{SW,th}$ is less than a tenth of $P_{SW,\mathrm{dyn}}$ there. On the other hand, $P_{SW,th}$ is an important factor in the distant tail, because the magnetopause there is fairly parallel to the solar wind flow and thus $P_{SW,\mathrm{dyn}}$ is small there. We will further discuss this point at the end of section 5.2.

3. Methodology

In this section, we first describe the magnetopause model which is fit to both data sets of the crossing positions and α values, and then describe how to fit the model to the data. The model magnetopause is assumed to be axisymmetric with regard to the X axis, and thus the spacecraft position is referred to as (x, R), where $R \equiv \sqrt{y^2 + z^2}$. The magnetopause model is ellipsoid-shaped, until it reaches the maximum distance from the X axis, and the distance of the model magnetopause from the focus of the ellipsoid, r_{model}, is expressed as

$$r_{\text{model}} = r_{\text{model}}(\theta) \equiv \frac{r_0(1+\varepsilon)}{1+\varepsilon\cos\theta}, \quad (2)$$

where θ refers to the solar zenith angle (aberrated $\sim 4°$, as stated above).

The ellipticity ε and the "minimum radius" r_0 are the model parameters. The position x and R of the model magnetopause are given as

$$x = x(\theta) = r_{\text{model}}(\theta)\cos\theta + x_0 \quad (3)$$

$$R = R(\theta) = r_{\text{model}}(\theta)\sin\theta, \quad (4)$$

where x_0 is the third parameter of the model, describing the X position of the focus of the ellipsoid. This parameter will be either fixed at zero (2-parameter model) or fit to the data (3-parameter model).

The model ellipsoid (equation 2) has a maximum R, R_{max}, at θ_t which satisfies

$$\cos\theta_t = -\varepsilon. \quad (5)$$

At this θ_t,

$$x_t \equiv x(\theta_t) = -r_0\frac{\varepsilon}{(1-\varepsilon)} + x_0 \quad (6)$$

$$R_{\text{max}} \equiv R(\theta_t) = r_0\sqrt{\frac{1+\varepsilon}{1-\varepsilon}} \quad (7)$$

hold true. For all $\theta > \theta_t$, our model magnetopause satisfies $R = R_{\text{max}}$ (cylindrical tail).

Given the shape of the magnetopause described above and given a crossing data point, one can calculate r_{obs}, which refers to the distance from the focus of the model ellipsoid to the crossing position, and r_{model}, as follows: $r_{\text{obs}} = \left[R_{\text{obs}}^2 + (x_{\text{obs}} - x_0)^2\right]^{1/2}$, $\theta = \tan^{-1}\left[R_{\text{obs}}/(x_{\text{obs}} - x_0)\right]$, and r_{model} is calculated by substituting the obtained θ into equation (2) (if $\theta \le \theta_t$) or by $r_{\text{model}} = R_{\text{max}}/\sin\theta$ (if $\theta > \theta_t$).

One can also calculate the model value of α, α_{model}, given the shape of the model magnetopause, as described above, and an observed α, α_{obs}. (More precisely, each α_{obs} in our data set was not directly observed but is estimated from a set of observed data). The procedure to calculate α_{model} corresponding to each α_{obs} is related to the procedure to estimate the α_{obs} from a set of observed data. Thus we first discuss the latter procedure, and then explain the former.

Each α_{obs} in our data set is determined so that it satisfies

$$\frac{B_{T,\text{lobe}}^2}{2\mu_0} = \rho v_{SW}^2\sin^2\alpha_{\text{obs}} + \frac{B_{T,SW}^2}{2\mu_0} + nk(T_{i,SW} + T_{e,SW}) \quad (8)$$

(e.g., equation (5) of PR96), where $B_{T,\text{lobe}}$ is the magnetic field strength observed by ISEE 2 in the lobe, and $B_{T,SW}$, n, $T_{i,SW}$, and $T_{e,SW}$ are the magnetic field strength, number density of ion, ion temperature, and electron temperature simultaneously observed by IMP 8 in the solar wind. It is noted that each α_{obs} has a corresponding position in the lobe where the observing spacecraft (ISEE 2) was located.

As we stated in section 1, the above procedure to calculate α_{obs} assumes that the lobe magnetic field is uniform from the satellite position to the magnetopause. As pointed out by *Roelof and Sibeck* [1995], this assumption could lead to some bias in the obtained α_{obs}, because the actual magnetic field lines in the lobe are more or less curved. $\nabla(B^2/2) = (\mathrm{B}\cdot\nabla)\mathrm{B} + \mathrm{B}\times\mathrm{rotB}$ holds true, and its first term is nonzero if the magnetic field lines are curved even if there is no current ($\mu_0^{-1}\mathrm{rotB}$) in the lobe. However, Figure 3 of PR96 shows that the effect of the field line curvature is not large: Their Figure 3 shows that the lobe magnetic field strength measured by ISEE 2 is fairly constant along the lines perpendicular to the tail magnetopause.

Another assumption in the above procedure to obtain α_{obs} is that the draping effect of the IMF over the magnetosphere is not included in (8). The draped IMF applies an anisotropic pressure to the magnetosphere. We appreciate its importance in determining the magnetopause shape [e.g., *Michel and Dessler*, 1970; *Sibeck et al.*, 1986], but the main purpose of this paper is to improve the magnetopause model in the class of axisymmetric models, and it is beyond the scope of this paper to extend the model to axi-asymmetric shapes.

To calculate α_{model} corresponding to each α_{obs}, we first define a plane which includes the spacecraft position (in the lobe) corresponding to the α_{obs} and the X axis, and we do all the following calculations in this plane. Next we draw a straight line from the spacecraft position to the model magnetopause so that the line makes a right angle to the magnetopause where the line crosses the magnetopause. Finally, we calculate α of the model magnetopause at the crossing point: This is the definition of α_{model}.

In this way, for any given set of model parameters (ε, r_0) or (ε, r_0, x_0), we can calculate r_{model} for each r_{obs}, and also α_{model} for each α_{obs}. Figure 1 illustrates the above explanation of the magnetopause model, and how to calculate r_{model} and α_{model}.

Having described the model magnetopause used in this study, the next question is how to fit the model to data. In order to make the following formulation meaningful in the context of statistics, we assume we are observing a joint distribution of r and α. That is, we will deal with the two-dimensional distribution of

$$\xi = \begin{pmatrix}\xi_1\\ \xi_2\end{pmatrix} \equiv \begin{pmatrix} r\\ \alpha\end{pmatrix}. \quad (9)$$

Next we assume that the residual of ξ from the model value $\xi_{\text{model}} = (r_{\text{model}}, \alpha_{\text{model}})^T$, where the superscript T means transposition from a row vector to a column vector, follows a (two-dimensional) Gaussian probability distribution. That is,

$$f_\xi(\xi) = \frac{1}{\sqrt{(2\pi)^2\,|\Sigma|}} \times \exp\left[-\frac{1}{2}(\xi - \xi_{\text{model}})^T\,\Sigma^{-1}\,(\xi - \xi_{\text{model}})\right], \quad (10)$$

where

$$\Sigma \equiv \begin{pmatrix}\sigma_{11}^2 & \sigma_{12}^2\\ \sigma_{21}^2 & \sigma_{22}^2\end{pmatrix} \quad (11)$$

is the error matrix of ξ, with σ_{ij}^2 meaning the covariance of $(\xi_i - \xi_{\text{model},i})$ and $(\xi_j - \xi_{\text{model},j})$, $|\Sigma|$ is the determinant of

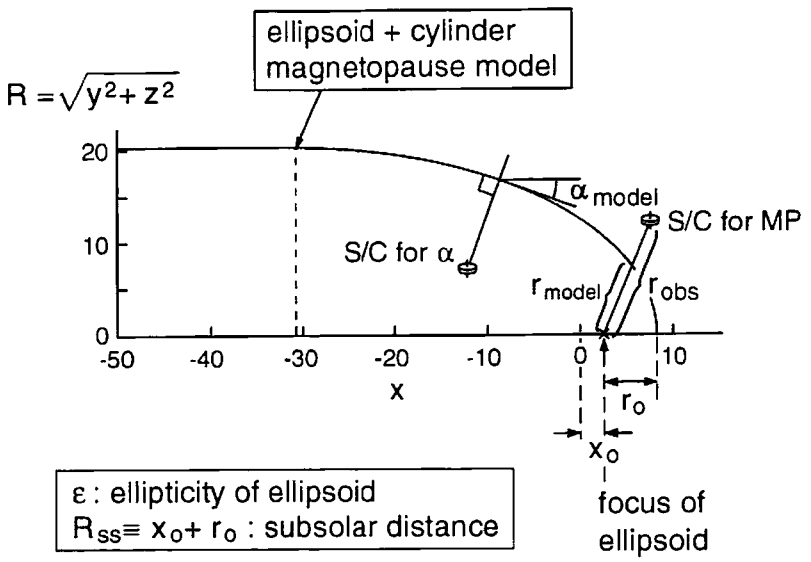

Figure 1. Illustrates the model magnetopause, and how to calculate $r_{\rm model}$ and $\alpha_{\rm model}$. See text for details.

Σ, and $(\xi - \xi_{\rm model})^T$ means the transposition of $(\xi - \xi_{\rm model})$ from a column vector to a row vector.

We further assume that $(r - r_{\rm model})$ and $(\alpha - \alpha_{\rm model})$ have no correlation, or in other words, that they are independent. This is a natural assumption, because the two observations are made independently. Then, $\sigma_{12} = \sigma_{21} = 0$, and

$$f_\xi(\xi) = f_r(r) \cdot f_\alpha(\alpha) \tag{12}$$

$$f_r(r) = \frac{1}{\sqrt{2\pi\sigma_r^2}} \exp\left\{-\frac{(r - r_{\rm model})^2}{2\sigma_r^2}\right\} \tag{13}$$

$$f_\alpha(\alpha) = \frac{1}{\sqrt{2\pi\sigma_\alpha^2}} \exp\left\{-\frac{(\alpha - \alpha_{\rm model})^2}{2\sigma_\alpha^2}\right\} \tag{14}$$

hold true, where $\sigma_{11} = \sigma_r$ and $\sigma_{22} = \sigma_\alpha$. Note the model has parameters, (ε, r_0) or (ε, r_0, x_0), which are to be fit to data, although not explicitly shown in these equations.

The strategy to find the optimal model parameters is to find those which maximize $E\Big(f_\xi(\xi)\Big)$, or equivalently $E\Big(\log f_\xi(\xi)\Big)$, where E refers to the "expectation" in the terminology of statistics. *Akaike* [1974] has shown that the following approximate equation generally holds true:

$$E\Big(\log f_\xi(\xi)\Big) \simeq \frac{1}{N}\sum_{j=1}^{N} \log f_\xi(\xi_{{\rm obs},j}) - \frac{k}{N}, \tag{15}$$

where the subscript "obs" refers to the observed data, and N refers to the number of the observed $\xi = (r, \alpha)^T$ data. As stated above, k refers to the number of model parameters. (In a strict sense, this approximation holds true only for model parameters which maximize the first term of (15), but it is all right to use this approximation at this stage, because the second term is unchanged while one tries to maximize the first term: the second term is fixed for a specific model, and is meaningful only when one compares different models.)

By substituting (12) into (15), we obtain

$$\begin{aligned} F &\equiv -E\Big(\log f_\xi(\xi)\Big) \\ &= \frac{1}{2}\left[1 + \log\left\{\frac{2\pi}{N}\sum_{m=1}^{N}(r_{{\rm obs},m} - r_{{\rm model},m})^2\right\}\right] \\ &+ \frac{1}{2}\left[1 + \log\left\{\frac{2\pi}{N}\sum_{n=1}^{N}(\alpha_{{\rm obs},n} - \alpha_{{\rm model},n})^2\right\}\right] \\ &+ \frac{k}{N} \end{aligned} \tag{16}$$

(see Appendix for the derivation). We minimize this F to obtain an optimal set of model parameters. Note that the second and fourth terms tend to decrease with increasing k, because models with a larger number of parameters become more adaptive to the data. On the other hand, the fifth (i.e., the last) term increases with increasing k. It is therefore unclear whether an increased k increases or decreases F, until an actual fit is made to the data set in question and F is evaluated. In other words, the data itself chooses the best model. We note here that the quantity $-2NE\Big(\log f_\xi(\xi)\Big)$ is called AIC (Akaike information criterion) and is widely used in statistics.

It is also important that r and α should always be paired for (15) to be valid. However, in the real world the number of r data, N_r, is different from that of the α data, N_α. Then, the smaller of N_r and N_α will be used for the number of $\xi = (r, \alpha)^T$, N, but in order to fully use the obtained data, we will adopt a technique similar to the bootstrap technique [e.g., *Kawano and Higuchi*, 1995]. That is, we (1) randomly sample one data point from the data set of r; (2) randomly sample one data point from the data set of α; (3) repeat (1) and (2) N times and obtain N data of $\xi = (r, \alpha)^T$; (4) fit a model to that data set. We repeat this procedure 500 times. (As stated above, $N = N_r$ when $N_r < N_\alpha$, and $N = N_\alpha$ when $N_r > N_\alpha$.) We note here that this procedure assumes that the r data and α data are sampled under the same solar wind conditions. As a result of repeating the procedure

500 times, we obtain 500 sets of resulting model parameters. Then, for each parameter, we use the median of the 500 values as its most probable estimation. We also use the 15.87–84.13 percentile range of the 500 values as the standard error of the parameter. As for the number of repetitions, statisticians' experience is that 25–200 is enough for obtaining the median and the standard error [e.g., *Efron and Tibshirani*, 1993], but we use 500 for the sake of safety, because our approach includes extracting N_r data from a data set of N_α data (when $N_r < N_\alpha$), which is not done in the usual bootstrap method.

In this way, we can calculate F for any given value of the model parameters, and thus can find its minimum point in parameter space. The actual minimization is done numerically because r_{model} and α_{model} are not linear functions of (ε, r_0) or (ε, r_0, x_0), and thus do not allow the analytical solution of

$$\frac{\partial F}{\partial \varepsilon} = 0 \tag{17}$$

and so on. We will use the so-called BFGS algorithm of the quasi-Newton method for the numerical minimization, whose concise explanation is found in the work of *Press et al.* [1992]. Since this algorithm is well established, we will not describe the actual minimization process but simply show the fitting results in the next section.

4. Data Analysis

4.1. Binning Study

First, we have divided the data with IMF $B_Z > 0$ nT into five bins according to $P_{SW,\mathrm{dyn}}$: the ranges of the pressure and the number of data in each bin are listed in Table 1, along with the median $P_{SW,\mathrm{dyn}}$ of each bin data. Then we have applied the above method to the data in each bin, assuming that they were obtained under the same $P_{SW,\mathrm{dyn}}$ condition and that the IMF does not affect the magnetopause shape. As a result, we have obtained optimum model parameters and F, along with their standard errors, for both the 2-parameter model and the 3-parameter model.

Figures 2–5 show the fitting results: Figure 2 shows $R_{ss} \equiv r_0 + x_0$, Figure 3 shows r_0, Figure 4 shows x_0, and Figure 5 shows ε, for the five bins. R_{ss} is the geocentric distance of the subsolar magnetopause. The top panel of each figure shows the results of fitting the 2-parameter model, and the bottom panel shows the results of fitting the 3-parameter model. The horizontal axes of the four figures are the same and show representative values of $P_{SW,\mathrm{dyn}}$ and their standard errors for the five bins. That is, for each bin, we have 500 resampled data sets, for each of which we can calculate the median $P_{SW,\mathrm{dyn}}$. Thus we can calculate the median of the 500 $P_{SW,\mathrm{dyn}}$ values. It is the representative value of $P_{SW,\mathrm{dyn}}$ for the bin. We can also calculate the 15.87–84.13 percentile range of the 500 $P_{SW,\mathrm{dyn}}$ values as the standard error of the above obtained representative $P_{SW,\mathrm{dyn}}$. The standard error is shown in each of Figures 2–5 as a horizontal error bar. The horizontal axis is drawn on a logarithmic scale. The lines in the figures are the results of fitting to entire data set at once, and will be discussed in section 4.2.

Table 1. Number of Events for IMF $B_Z > 0$ (nT), in Solar Wind Dynamic Pressure Bins

$P_{SW,\mathrm{dyn}}$ Range, nPa			Number of Crossing Data	Number of Flaring Angle Data	Median $P_{SW,\mathrm{dyn}}$, nPa
	$<$	$2^{-0.5}$	13	285	0.62
$2^{-0.5}$	–	$2^{0.5}$	69	1183	1.1
$2^{0.5}$	–	$2^{1.5}$	100	947	2.0
$2^{1.5}$	–	$2^{2.5}$	58	331	3.7
	$\geq$	$2^{2.5}$	9	145	6.7

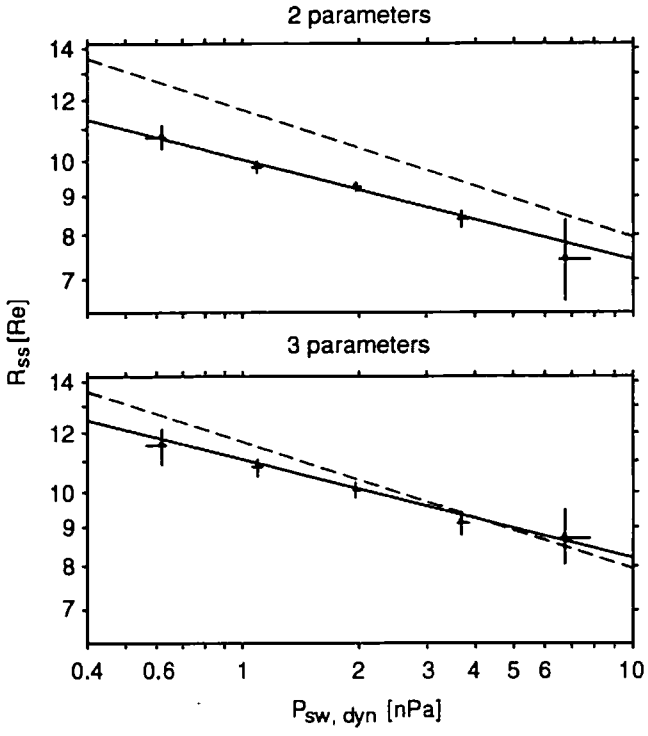

Figure 2. Shows geocentric distance of subsolar magnetopause, R_{ss}, in (top) the 2-parameter model and (bottom) the 3-parameter model of the magnetopause, fit to the five bins listed in Table 1. Each bin is associated with different range of solar wind dynamic pressure, $P_{SW,\mathrm{dyn}}$, as shown in the horizontal axis. More detail is given in section 4.1. The solid lines show (top) the 2-parameter and (bottom) the 3-parameter model, fit to all data. Table 2 lists the parameters of the models. See section 4.2 for details of the lines. The dashed lines show R_{ss} of *Petrinec and Russell* [1996].

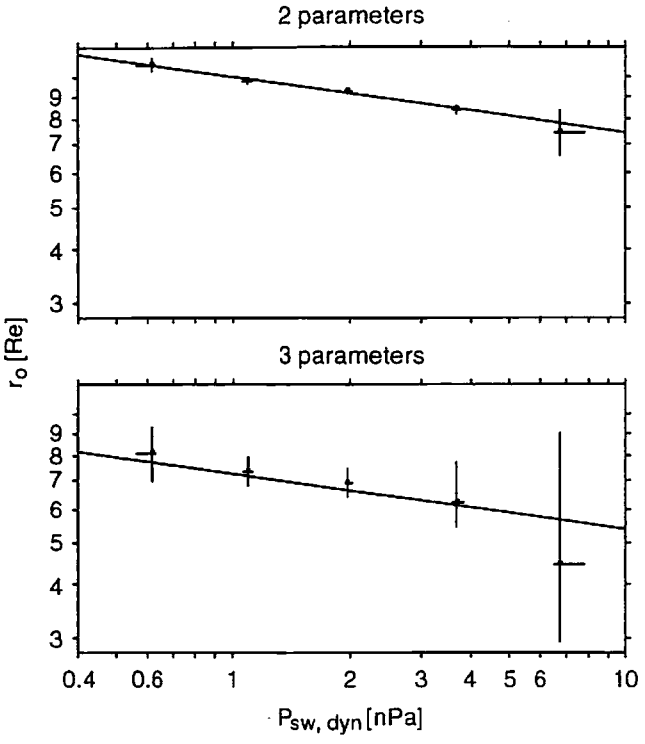

Figure 3. Same as Figure 2, except that the "minimum radius of the ellipsoid," r_0, is shown.

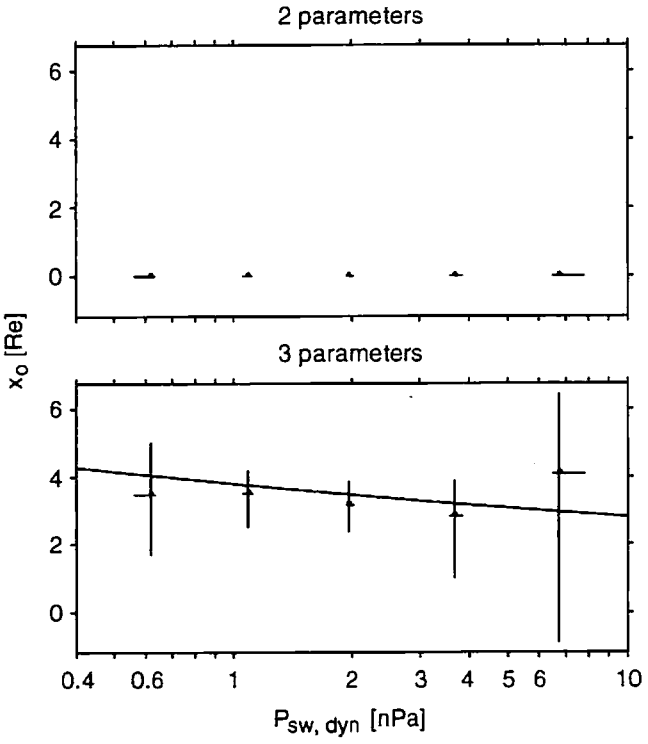

Figure 4. Same as Figure 2, except that the X position of the focus of the ellipsoid, x_0, is shown.

Figure 3 shows the $P_{SW,\mathrm{dyn}}$ dependence of r_0. The vertical axis is drawn on a logarithmic scale. For both models, the bin-wise fit r_0 values are well aligned in the figure, as R_{ss} values are in Figure 2. Note in Figure 3 (and in Figure 5 below) that the error bars in the 3-parameter model (bottom) are much longer than corresponding error bars in the 2-parameter model (top). This indicates that the reliability/precision of already existing fit parameters tends to decrease with the addition of an extra parameter, as we stated in the last paragraph of section 1.

Figure 4 shows x_0 as a function of $P_{SW,\mathrm{dyn}}$. The vertical axis is plotted on a linear scale. In the top panel, x_0 is always zero, which is a matter of course, because in the 2-parameter model x_0 is fixed to zero. In the bottom panel, that is, in the 3-parameter model, we find that the standard errors in x_0 are so large in general that the $P_{SW,\mathrm{dyn}}$ dependence of x_0 is not uniquely determined from the data. However, since R_{ss} and r_0 show a power law dependence on $P_{SW,\mathrm{dyn}}$, $x_0 = R_{ss} - r_0$ can also be assumed to have a power law dependence on $P_{SW,\mathrm{dyn}}$.

Figure 5 shows ε as a function of $P_{SW,\mathrm{dyn}}$. The vertical axis is linear. In both panels, it is clear that ε decreases with increasing $P_{SW,\mathrm{dyn}}$. This means that the magnetopause shape is not self similar under different $P_{SW,\mathrm{dyn}}$. This point will be discussed in section 5.

As we described above, the goodness of the two models can be judged by comparing the quantity F (equation 16) for the two models. Here we write F for the 2-parameter model as $F(2)$, and F for the 3-parameter model as $F(3)$, and show in Figure 6 $F(2) - F(3)$ for the five $P_{SW,\mathrm{dyn}}$ bins. In (16), k is set to 2 for the 2-parameter model, and 3 for the 3-parameter model. Figure 6 shows that the median, or in other words, the statistical estimate, of $F(2) - F(3)$ is positive for all five bins. This means that the 3-parameter model

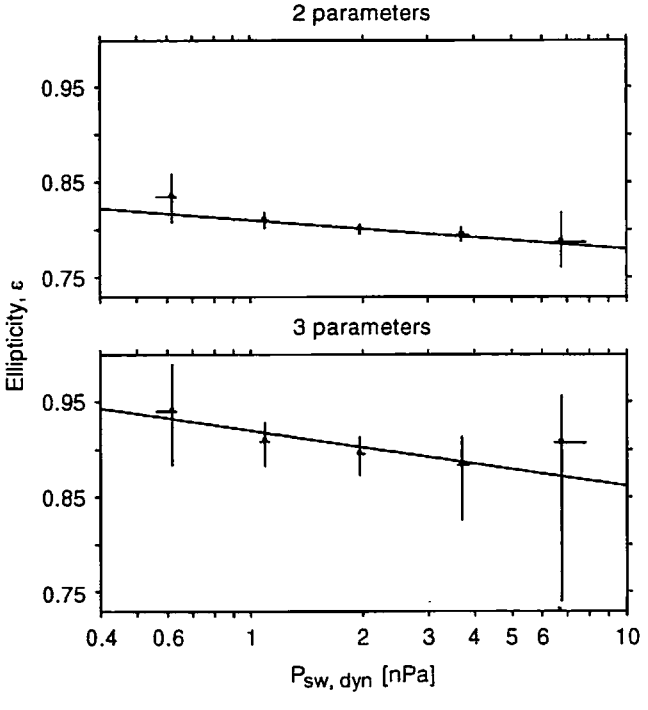

Figure 5. Same as Figure 2, except that the ellipticity of the ellipsoid, ε, is shown.

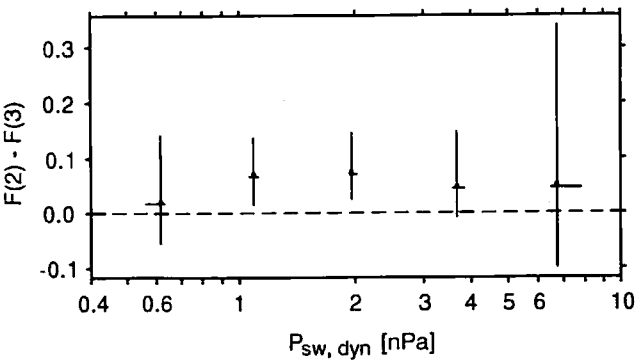

Figure 6. Shows the difference between the 2-parameter model and the 3-parameter model in the value of the F quantity of (16), for the five bins.

fits better than the 2-parameter model in general. However, the error bar, or in other words the 68% confidence interval of the estimate, crosses the zero line for the first, fourth, and fifth smallest $P_{SW,\mathrm{dyn}}$ bins. Thus $F(2)-F(3)$ is not significantly positive for these bins. Because different bins provide a difference in the order of significance, it is unclear if the data, in whole, suggest using the 2-parameter model or the 3-parameter model.

4.2. Using All Data

In the preceding section we have found that there are $P_{SW,\mathrm{dyn}}$ dependences in the bin-wise fit model parameters. In this section we explicitly use this information to express x_0, r_0, and ε as functions of $P_{SW,\mathrm{dyn}}$, and determine the coefficients of the functions from data fitting. This enables us to express the magnetopause shape in a bin-independent form, and enables evaluating the goodness of the 2-parameter model versus the 3-parameter model based on all available data.

Because Figure 2 suggests a power law dependence of Rss on $P_{SW,\mathrm{dyn}}$, we express the relation as

$$R_{ss} = A_c \left(\frac{P_{SW,\mathrm{dyn}}}{p_0} \right)^{B_c} , \tag{18}$$

where A_c and B_c are parameters to be fit to data, while p_0 is not a fitting parameter but a normalization quantity. We set p_0 as a nominal value of $P_{SW,\mathrm{dyn}}$, that is,

$$p_0 = 2 \text{ nPa} . \tag{19}$$

Similarly, since Figure 3 suggests a power law dependence of r_0 on $P_{SW,\mathrm{dyn}}$, we express the relation as

$$r_0 = C_c \left(\frac{P_{SW,\mathrm{dyn}}}{p_0} \right)^{B_c} , \tag{20}$$

where B_c and C_c are parameters to be fit to data. We assume here that R_{ss} and r_0 have the same coefficient B_c. This simplifies the calculation of x_0 from R_{ss} and r_0:

$$x_0 = (A_c - C_c) \left(\frac{P_{SW,\mathrm{dyn}}}{p_0} \right)^{B_c} , \tag{21}$$

and it would be natural to think that the two quantities x_0 and r_0, closely related to the size of the subsolar magnetopause, have the same $P_{SW,\mathrm{dyn}}$ dependence. Of course, this assumption must be consistent with the actual observations, which we will test below.

The above equation for x_0 is, of course, for the 3-parameter model: For the 2-parameter model, x_0 is always fixed to zero, and thus $r_0 = R_{ss}$.

Finally, as to ε, we assume the following relation:

$$\varepsilon = D_c + E_c \log \left(\frac{P_{SW,\mathrm{dyn}}}{p_0} \right) . \tag{22}$$

Using this equation corresponds to drawing a best fit line to a panel of Figure 5. A linear fit is the simplest, and we do not see any special $P_{SW,\mathrm{dyn}}$ dependence in Figure 5 which requires fitting more complicated curves.

In summary, in the 2-parameter model, the model parameters to be fit to data are now not (ε, r_0) but (A_c, B_c, D_c, E_c), and in the 3-parameter model, the model parameters to be fit to data are now not (ε, r_0, x_0) but $(A_c, B_c, C_c, D_c, E_c)$. That is, the 2-parameter model actually has four model parameters now, and the 3-parameter model actually has five model parameters now. Still, we will use the terms "2-parameter model" and "3-parameter model," for the sake of convenience.

The actual procedure to fit the models to the data is very similar to that described in section 3. That is, for example when $N = N_r < N_\alpha$ (where N_r and N_α are now the total number of the r data and that of the α data, and $N_r < N_\alpha$ is actually the case for our data set (N_r=249, N_α=2891)), we (1) randomly sample one data point from the data set of r; (2) sample one data point from the data set of α which is associated with the same $P_{SW,\mathrm{dyn}}$ value as that associating the r data sampled in (1); (3) repeat (1) and (2) N times and obtain N data of $\xi = (r, \alpha)^T$; (4) fit a model to that data set. We repeat this procedure 500 times.

Note that every ξ can now have different $P_{SW,\mathrm{dyn}}$. For each ξ, its corresponding $P_{SW,\mathrm{dyn}}$ is put into equations (18) through (22) to obtain (ε, r_0) or (ε, r_0, x_0), and then r_{model} and α_{model} are calculated. With the N sets of ξ, r_{model}, and α_{model}, F in (16) is calculated. We set $k = 4$ for the 2-parameter model, while $k = 5$ for the 3-parameter model, in (16).

Step (2) above requires elaboration. As explained in section 3, r and α should always be paired, and should be regarded as those observed under the same solar wind conditions. Since the r and α are in fact obtained independently, there is no pair of r and α which are taken under exactly the same $P_{SW,\mathrm{dyn}}$. Thus the following approximating procedure is taken; (for example) when $N_r < N_\alpha$, there is more than one α measurement that can be assigned to each r datum. We sort the r data according to associated $P_{SW,\mathrm{dyn}}$, in an ascending order, and use the mean values of each two neighboring values of $P_{SW,\mathrm{dyn}}$ as border values to group the α

data. For example, if the i-th r data, r_i, is surrounded by the two border $P_{SW,\mathrm{dyn}}$ values P_l and P_u, then all α data associated with $P_{SW,\mathrm{dyn}}$ between P_l and P_u are able to make a pair with r_i, and one of them is randomly selected each time r_i is selected in the above procedure (1). Then, the average of the two values of $P_{SW,\mathrm{dyn}}$ associated with the selected r data and the α data is used as that associated with this ξ.

In this way, we have fit the parameters (A_c, B_c, D_c, E_c) (2-parameter model) or (A_c, B_c, C_c, D_c, E_c) (3-parameter model) to all data. The results are summarized in Table 2. In addition, solid lines in Figures 2 through 5 illustrate the results. The solid lines in Figure 2 show (18) with A_c and B_c listed in Table 2. The dashed lines will be discussed in section 5. The solid lines in Figure 3 show (20) with B_c and C_c listed in Table 2. The solid lines in Figure 4 show (21) with A_c, B_c, and C_c listed in Table 2. The solid lines in Figure 5 show (22) with D_c and E_c listed in Table 2.

In Figures 2–5, the lines fit to all data pass through the error bars of the bin-wise fit points. This justifies the assumptions introduced in (18) through (22).

5. Discussion

5.1. Model Shape in the Region Covered by Data

The bottom row of Table 2 shows $F(2) - F(3)$ calculated using all data. Even taking into account the standard error, or in other words, with the confidence level of 68%, $F(2)-F(3)$ is positive. That is, $F(3)$ is significantly smaller than $F(2)$. Thus we can objectively decide now that the 3-parameter model is better than the 2-parameter model. Inclusion of the off-geocentric focus of the ellipsoid is meaningful when fit to the data. In the following we only look at the 3-parameter model, fit to all data, whose parameters are shown in Table 2.

It is of interest to see how the observed data are actually fit by the model. Because it is difficult to show all data associated with a wide variety of $P_{SW,\mathrm{dyn}}$, we use the five binned subsets used in section 4.1 and show how they are fit. Figures 7a through 7e show the observed magnetopause crossing positions and the model magnetopause shape for the five bins. The model curves are from the (3-parameter) model fit to all data, not from the models fit to each bin data. For comparison, we have also plotted the magnetopause shape of RS93 and that of PR96 for IMF $B_Z = 2.6$ nT. This quantity 2.6 is the median value for our data set, as is listed in Table 2. Because the other two models are dependent on B_Z, we use this median value so that we could expect closest predictions.

It is noted in Figure 7 that, when $P_{SW,\mathrm{dyn}}$ is small, our model tends to return a subsolar magnetopause closer to the Earth than the other models. This tendency is also found in the bottom panel of Figure 2. That is, the dashed line in the bottom panel of Figure 2 shows R_{ss} of PR96, and the dashed line shows larger values than the solid line for $P_{SW,\mathrm{dyn}} < 4.2$ nPa. However, if the error bars of the PR96 model are comparable to those of our model, the error bars would overlap. In addition, Figures 7a through 7e show that, in the dayside region, the distribution width of the observed data is comparable to the differences in the three curves. Thus, in the dayside region, the difference in the three models are not extremely large.

We also note in the bottom panel of Figure 2 that the slope of the solid line (our model) is less steep than that of the dashed line [*Petrinec and Russell*, 1993, 1996], which is $-1/6$. (They a priori fixed the slope to $-1/6$, according to a theoretical expectation.) As shown in Table 2, the slope is -0.130 with a standard error range (i.e., 65% confidence interval) of -0.142 to -0.119. In fact, even the 3-sigma range (i.e., 99.7% confidence interval) (-0.161 to -0.097) does not include $-1/6$. This difference from $-1/6$ may therefore be real.

A possible explanation for the above difference is the ef-

Table 2. Results of Fitting to All Data

Parameter/Quantity	Unit	Estimate	Standard Error Range		
Data median $P_{SW,\mathrm{dyn}}$	nPa	1.97	1.90	—	2.08
Data median IMF B_Z	nT	2.6	2.5	—	2.8
2-parameter model, A_c	R_E	9.16	9.07	—	9.25
2-parameter model, B_c	NoDim	−0.131	−0.148	—	−0.115
2-parameter model, C_c	R_E	9.16	9.07	—	9.25
2-parameter model, D_c	NoDim	0.801	0.797	—	0.805
2-parameter model, E_c	NoDim	−0.013	−0.020	—	−0.007
3-parameter model, A_c	R_E	10.10	9.98	—	10.24
3-parameter model, B_c	NoDim	−0.130	−0.142	—	−0.119
3-parameter model, C_c	R_E	6.64	6.36	—	6.96
3-parameter model, D_c	NoDim	0.902	0.890	—	0.913
3-parameter model, E_c	NoDim	−0.025	−0.032	—	−0.019
$F(2) - F(3)$	NoDim	0.10	0.06	—	0.15

NoDim, nondimensional.

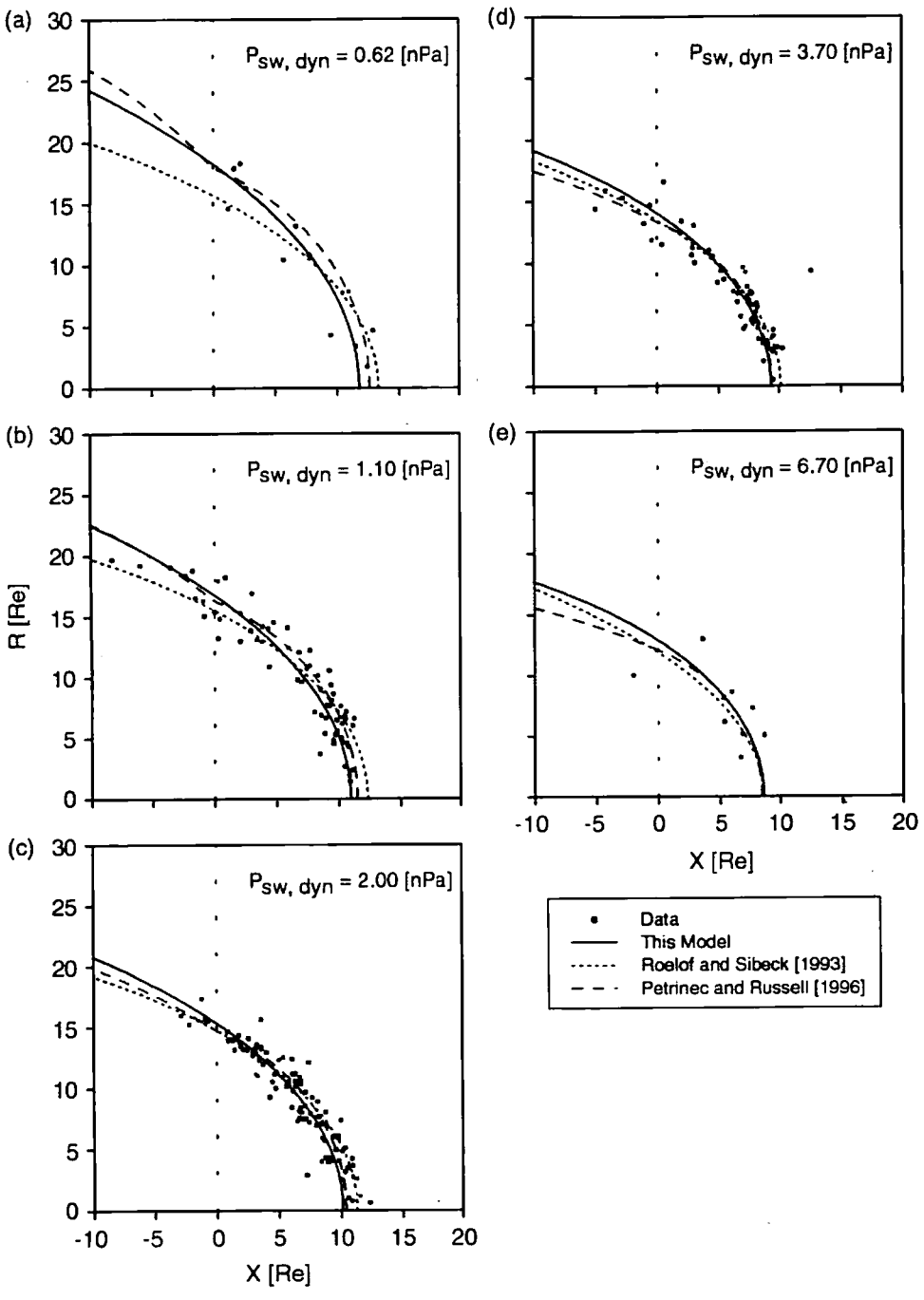

Figure 7. Comparison of the observed magnetopause crossings and the 3-parameter model magnetopause fit to all data. The five panels correspond to the five bins of Table 1. Models by *Roelof and Sibeck* [1993] and *Petrinec and Russell* [1996] for $B_z = 2.6$ nT are also shown. See text for details.

fect of $P_{SW,\mathrm{dyn}}$ on the post cusp reconnection rate. *Scurry and Russell* [1991] suggested that a large $P_{SW,\mathrm{dyn}}$ enhances the subsolar reconnection rate when the IMF is southward. On the other hand, when the IMF is northward, it is widely believed that reconnection takes place near the polar cusp [e.g., *Kessel et al.*, 1996, and references therein]. If a large $P_{SW,\mathrm{dyn}}$ enhances the cusp reconnection rate when the IMF is northward, that could then increase the closed magnetic flux in the dayside magnetosphere via simultaneous reconnection at northern and southern cusps [*Song and Russell*, 1992]. That would make R_{ss} larger than that when there is no cusp reconnection for a large $P_{SW,\mathrm{dyn}}$, leading to the less steep slope noted above.

We note that the RS93 model is more or less against this possibility. That is, Figure 17b of RS93 shows that the absolute value of the power law constant in their model increases as the IMF B_z increases from a negative value toward a positive value. This is opposite to what is expected from our

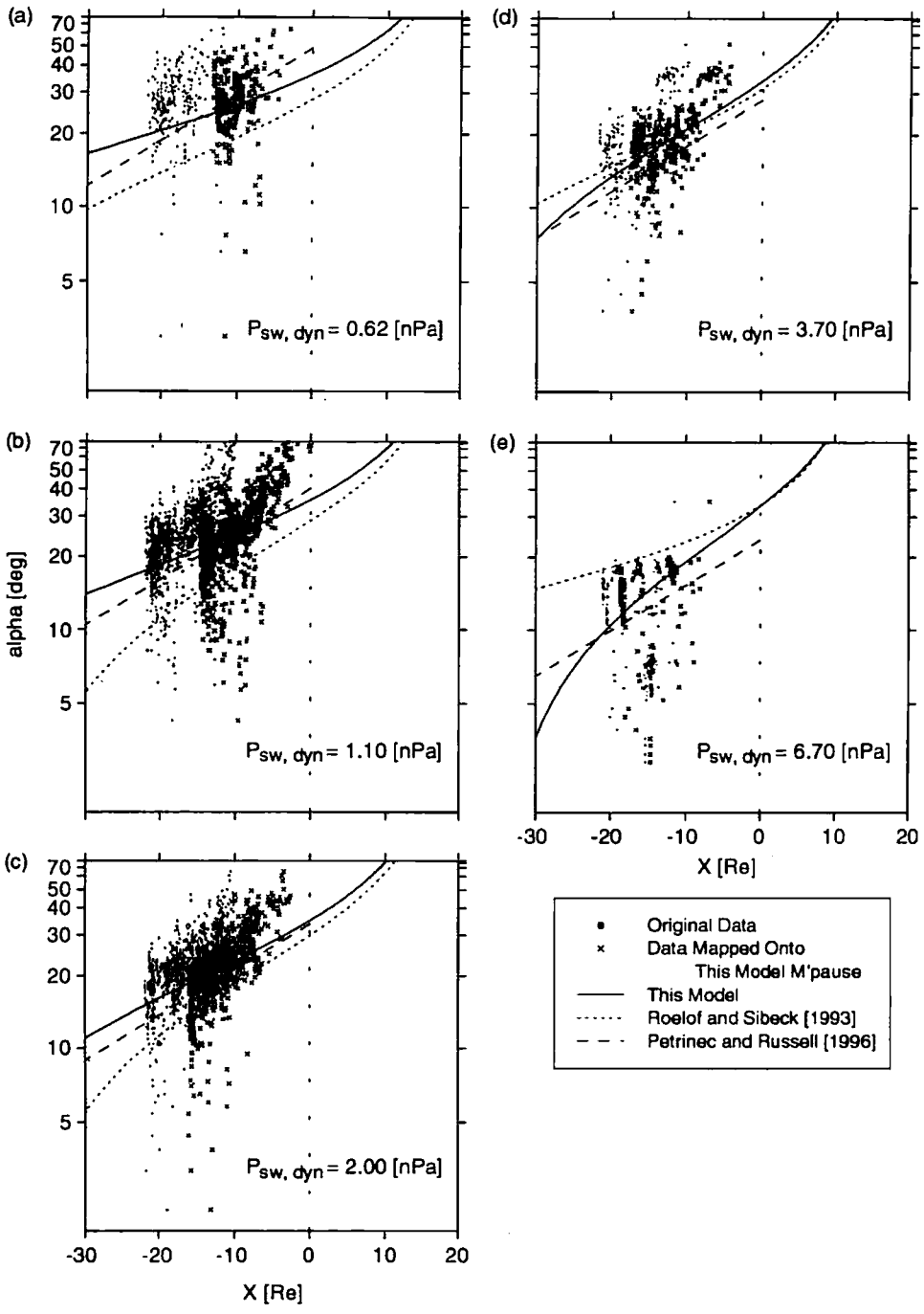

Figure 8. Comparison of the flaring angles of the magnetopause, α, estimated from the pressure balance between the solar wind and the lobe, and the modeled α. Our 3-parameter model fit to all data, *Roelof and Sibeck*'s [1993] model, and *Petrinec and Russell*'s [1996] model are shown. The five panels correspond to the five bins of Table 1. See text for details.

above conjecture. We think it is worthwhile to study whether the same tendency is found or not from our data, by including IMF B_z as a control factor in our model. This is a topic of future research.

Figures 8a through 8e show α_{obs} and α_{model} values. The scaling of the vertical axis, showing α, are arranged so that the PR96 model is expressed by straight lines in Figure 8. That is, the vertical scaling is linear to $\log(\sin^2 \alpha)$, as in Figure 1c of PR96. (Note in Figure 8 that the lines of PR96 are shown only in the region of $X < 0$. We have skipped the $X > 0$ part, because it has a different mathematical form.) The bottom and top of the panels correspond to $\alpha = 1.9°$ and $\alpha = 90°$. The dots show α_{obs} values at the positions of the satellite. The crosses show them mapped onto our model magnetopause, as illustrated in Figure 1. Of course, the value of α_{obs} is unchanged by this mapping.

We note in Figures 8a, 8b, and 8e that the curves of the RS93 model miss the region where our α_{obs} values are mainly distributed: The RS93 model gives α predictions smaller (larger) than the data in Figures 8a and 8b (Figure 8e). The RS93 model is therefore inconsistent with our α_{obs} values when $P_{SW,dyn}$ is much higher or lower than its median value. Their model is consistent with their data where there is coverage, but when we look at the distribution of their data, we find that the number of data points is small in this region. If we count the number of data points at $X < -10\ R_E$, $P_{SW,dyn} < 1$ nPa, and IMF $B_z > 0$ nT in Figure 8a of RS93, we obtain 2; if we count the number of data points at $X < -10\ R_E$, $P_{SW,dyn} > 4$ nPa, and IMF $B_z > 0$ nT in Figure 8b of RS93, we obtain 7. Many more crossings at these ranges are necessary for a significant comparison with α_{obs} values. In addition, at $X < -10\ R_E$, $P_{SW,dyn} > 4$ nPa, and IMF $B_z > 0$ nT, we can see the seven crossing points located within their model magnetosphere on average. This implies some difference between their observations and their model at this range, although more data points are necessary for significant information.

We also note in Figure 8 that the PR96 model and our model run near the center of the data distributions in all of the five figures, which is natural because the two models are fit to the same data set of α_{obs}. Still, if we look in more detail, in Figure 8a (Figures 8d and 8e) our model predicts smaller (larger) α than the PR96 model does in the region of the crosses. This is because our model is also fit to the magnetopause-crossing data at the same time. In Figures 8a through 8e, the curve of our model reaches the top border of the figure ($\alpha = 90°$) at the subsolar point and is "anchored" there due to the requirement that the model must fit well with the magnetopause-crossing data. The slope of the curve is also partly controlled by the crossing data where they exist, mainly at $X > 0$. Thus our model cannot be closer to the center of the data distribution than the PR96 model. For example in Figure 8a, our model cannot be located as high as theirs at $X = 0$, because the part at $X > 0$ is confined by the magnetopause-crossing data. Their model can be located higher in Figure 8 at $X = 0$ than ours, because α can discretely jump at $X = 0$ (see, e.g., Figure 7a). This difference in α at $X = 0$ is partly compensated by the gentler slope of our model curve at $X < 0$ than theirs, but our α_{model} is still lower than theirs at the region of the data distribution (crosses).

Another difference between our model and the PR96 model apparent in Figure 8 is that the slope of the curves is always the same in their model (see the same slope of the dashed lines in the five panels), while it becomes steep with increasing $P_{SW,dyn}$ in our model (for example, it is more steep in Figure 8e than in Figure 8a). A steep slope means that the tail reaches its asymptotic state rapidly with increasing distance from the Earth. In the PR96 model, the slope is assumed to be independent of $P_{SW,dyn}$.

5.2. Extrapolated Model Shape

Although our model was developed for the region from the subsolar point to the near-Earth tail, it is interesting and important to see if the model could be applied to further downtail distances. It is believed that a well-constructed model of the magnetopause developed from observations can be extrapolated farther downstream than is supported by observations and still provides a reasonable estimate for the shape of the magnetotail, unless the actual magnetopause shape bends away from the modeled shape in the unobserved region. (Note it is our assumption that there is no such bend. This point will be further discussed near the end of this subsection.)

Figures 9a through 9e show the three model magnetopause shapes, for the same set of $P_{SW,dyn}$ and IMF B_Z as in Figures 7 and 8, but in wider X range, that is, in the region of $X \geq -140\ R_E$. The RS93 model is drawn up to the point where its tail radius reaches the maximum. When one looks at the entire shape of the models, our model is similar to the PR96 model. We also note that the RS93 model gives a smaller (larger) tail radius than the other two models do when $P_{SW,dyn}$ is small (large). Such a difference in the low-$P_{SW,dyn}$ (high-$P_{SW,dyn}$) case is apparent in Figure 9a (Figure 9e).

When one looks at the shape of the near-Earth tail magnetopause ($-10\ R_E \leq X \leq 0\ R_E$) in Figure 7, one would find basically the same similarity/difference among the three models as stated above. However in Figure 7e, our model looks rather closer to the RS93 model than to the PR96 model. (However, as one sees in Figure 9e, the similarity of the former two models only lasts until $X \simeq -20\ R_E$, and farther than that our model approaches the PR96 model.) The difference between our model and the PR96 model for high $P_{SW,dyn}$ in the near-Earth tail may come from the assumption of the PR96 model that the slope of the α curve in Figure 8 is independent of $P_{SW,dyn}$. That is, in Figure 8e, it is possible to draw a straight line running though the data distribution, with a steeper slope than that of the line of PR96, and with a larger α at $X = 0$. This larger α around $X = 0$ would cause a more flared tail in the near-Earth region, as in our model. (The difference in the slopes of $\alpha(x)$ between our model and the PR96 model causes a very small difference in the asymptotic tail radii of the two models, as seen in Figure 9e, because the asymptotic radius is related to the integral of $\tan\alpha(x)$ with x, thus is related to the area between the curve of $\alpha(x)$ and $x = 0$.)

The asymptotic tail radius in our model is given by (7), which indicates that R_{max} has the same $P_{SW,dyn}$ dependence as r_0 on condition that ε is independent of $P_{SW,dyn}$. However, ε is in fact dependent on $P_{SW,dyn}$, as shown in Figure 5 and Table 2. That is, our magnetopause model is not self-similar with regard to $P_{SW,dyn}$. We want to study the difference in the dependence on $P_{SW,dyn}$ of R_{ss} and R_{max}, but substituting (22) into (7) does not provide an equation such that R_{max} is proportional to the power of $P_{SW,dyn}$. However, if we return to the original data, we can fit a power law function to them. Instead of using (22), we then use

$$R_{max} = G_c \left(\frac{P_{SW,dyn}}{p_0} \right)^{H_c} \tag{23}$$

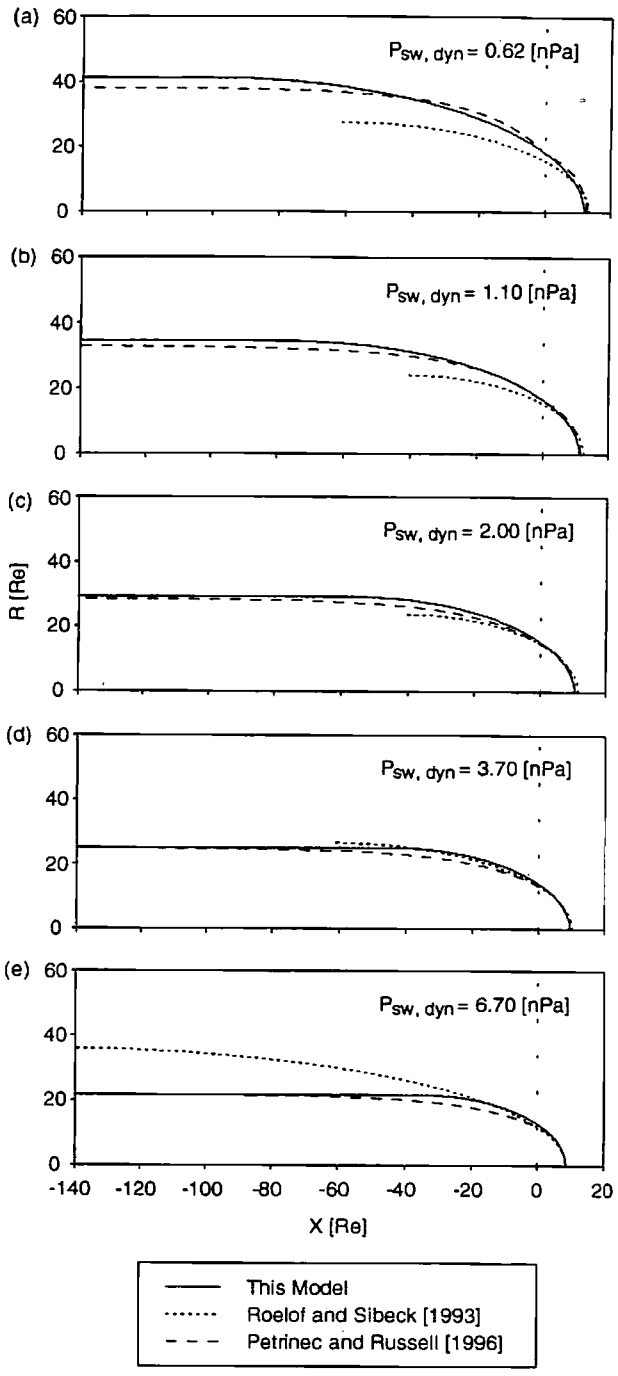

Figure 9. Shows the modeled magnetopause shapes, the same as in Figure 7 but for wider X range.

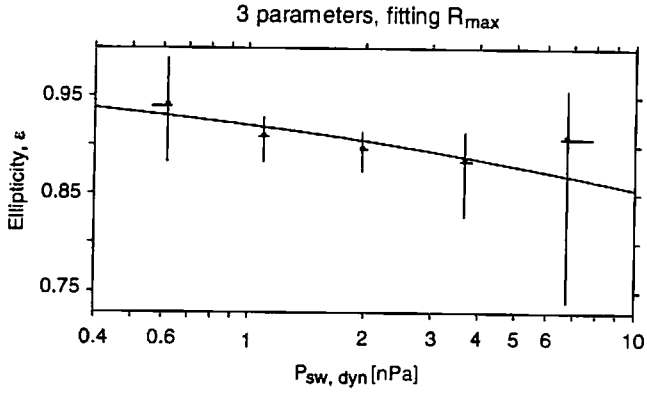

Figure 10. Same as Figure 5, except that the superposed curve comes from the model whose parameters are enlisted in Table 3.

and fit $(A_c, B_c, C_c, G_c, H_c)$ to all data. The result of doing so is summarized in Table 3.

The bottom row of the table shows the difference in the F quantity between the two models (3-parameter model with $(A_c, B_c, C_c, D_c, E_c)$, or that with $(A_c, B_c, C_c, G_c, H_c)$). Since each F value is close to 5 (not shown), the difference is negligible. That is, the two models are almost equivalent. Another proof of this equivalence is the great similarity of A_c, B_c, and C_c in Table 2 and 3. We have confirmed that we get almost the same figures as Figures 2, 3, and 4 for R_{ss}, r_0, and x_0 (not shown). In the $(A_c, B_c, C_c, G_c, H_c)$ model ε is calculated by

$$\varepsilon = \frac{R_{\max}^2 - r_0^2}{R_{\max}^2 + r_0^2}, \tag{24}$$

which is the algebraic deformation of (7), and r_0 and $R_{\max}$ are calculated by (20) and (23). Figure 10 shows the model curve of ε in this model, in the same format as that of Figure 5. The model curve is similar to that in Figure 5. In this way, the two types of the 3-parameter models are almost equivalent, and thus one can use either type (the 3-parameter model in Tables 2 or 3).

Having confirmed that the two types are equivalent, we resume the discussion of the $P_{SW,\mathrm{dyn}}$ dependence of $R_{\max}$. As one can see in Table 3, $R_{\max}$ is proportional to $P_{SW,\mathrm{dyn}}{}^{-0.267}$. Since R_{ss} is proportional to $P_{SW,\mathrm{dyn}}{}^{-0.130}$, as is shown in the same table, $R_{\max}$ is much more affected by $P_{SW,\mathrm{dyn}}$ than R_{ss} is. This feature was also found by PR96. Looking at their Figure 10 and thinking of our

Table 3. Results of Another Way of Fitting to All Data

Parameter/Quantity	Unit	Estimate	Standard Error Range		
3-parameter model, A_c	R_E	10.12	9.98	—	10.24
3-parameter model, B_c	NoDim	−0.130	−0.142	—	−0.119
3-parameter model, C_c	R_E	6.62	6.33	—	6.94
3-parameter model, G_c	R_E	29.5	28.9	—	30.4
3-parameter model, H_c	NoDim	−0.267	−0.307	—	−0.228
$F(A_c, B_c, C_c, G_c, H_c) - F(A_c, B_c, C_c, D_c, E_c)$	NoDim	−0.001	−0.004	—	0.001

standard error range of the power law constant, $-0.307 \sim -0.228$, the power law constant itself is also similar to that of PR96, and to that of *Lui* [1986], who obtained it from 12 magnetopause crossings near $X = -17.5\ R_E$ observed by the IMP 6 spacecraft (which had an apogee of 32.2 R_E).

On the other hand, as discussed by *Petrinec and Russell* [1995], *Roelof and Sibeck* [1995], and PR96, the tail radius of the RS93 model at $-20\ R_E < X < -15\ R_E$ shows much less dependence on $P_{SW,\mathrm{dyn}}$ than PR96 and our model do. As seen in Figure 2 of *Roelof and Sibeck* [1995], the crossing data of RS93 for high $P_{SW,\mathrm{dyn}}$ are closer to the PR96 model than to the RS93 model, and vice versa for low $P_{SW,\mathrm{dyn}}$. Their data distribution for low $P_{SW,\mathrm{dyn}}$ may be biased toward a small radius because of the limited orbital coverage of the satellites they used, as discussed by *Petrinec and Russell* [1995]. That is, the data set of RS93 consists of magnetopause crossings observed by many satellites, and many of the satellites did not reach the area where the PR96 model and our model magnetopause are located for low $P_{SW,\mathrm{dyn}}$, because of their apogee limitation. (For example, ISEE 1 and 2, AMPTE CCE and IRM had an apogee less than 30 R_E.) Another possibility is the effect of the curvature of the lobe field lines, which we discussed in section 3. Even though it is found to be small for nominal $P_{SW,\mathrm{dyn}}$ (see Figure 3 of PR96), it would increase as the X dependence of the tail radius becomes large, and that happens as $P_{SW,\mathrm{dyn}}$ decreases. However we do not know to what extent it is so (the curvature effect might be very small even when $P_{SW,\mathrm{dyn}}$ is small), and the curvature effect does not answer the question why the data of RS93 are closer to the PR96 model than to the RS93 model for high $P_{SW,\mathrm{dyn}}$. In any case, the number of crossing data at $X < -10\ R_E$ during very high or low $P_{SW,\mathrm{dyn}}$ is quite small in the data set of RS93, as stated earlier in this section; many more crossing locations are needed for a significant comparison with our data set of α_{obs}.

In Figure 9, one can find that x_t, the x position where the tail radius reaches a maximum, approaches the Earth as $P_{SW,\mathrm{dyn}}$ increases. This tendency is a matter of course if the magnetopause shape is self-similar with regard to $P_{SW,\mathrm{dyn}}$ but, as stated above, our magnetopause model is not such. As another support of this not being a matter of course, x_t of the RS93 model, which is not self-similar either, shows a $P_{SW,\mathrm{dyn}}$ dependence much different from ours, as one can see in the same figure. Although this $P_{SW,\mathrm{dyn}}$ dependence of x_t belongs to the extrapolated information (because x_t lies in the region of no data point), its systematic behavior implies it has some reality. In addition, as discussed by PR96, the asymptotic tail radius of our model (and the PR96 model, because the two are similar there), which also belongs to the extrapolated information, is in fact consistent with the ISEE 3 distant-tail observations reported by *Slavin et al.* [1985] (although *Fairfield* [1992] reported a smaller estimate): Slavin et al. obtained the radius of $30\pm3\ R_E$ from statistical distribution of the magnetopause crossings, while Fairfield suggested a radius of $24\pm2\ R_E$ based on the relative frequency of observations of the magnetosheath and magnetotail in the region. (As listed in Table 3 (as G_c), our asymptotic radius for $P_{SW,\mathrm{dyn}} = 2$ nPa is $\sim 30\ R_E$.)

Sibeck et al. [1986] summarized previously reported distant magnetopause crossings. Their summary (their Table 1) shows the radius along the Y axis to be 20 to 38 R_E and the radius along the Z axis to be 19 to 30 R_E for $X < -60\ R_E$. These ranges include the asymptotic tail radius of our model for $P_{SW,\mathrm{dyn}} = 2$ nPa ($\sim 30\ R_E$). *Nakamura et al.* [1997] presented statistics of the tail radius at $X = -83$ to $-210\ R_E$ observed by the Geotail spacecraft. They obtained a result that the quiet time tail had the average Y radius of 35 R_E and the average Z radius of 23 R_E. The asymptotic tail radius of our model for $P_{SW,\mathrm{dyn}} = 2$ nPa lies between these two numbers. In short, the asymptotic radius we have obtained is consistent with many of the actual observations in literature.

As we mentioned at the beginning of this subsection, it is our assumption throughout this subsection that the ellipsoid-plus-cylinder shape can successfully approximate the entire shape of the magnetopause from the subsolar point to the asymptotic tail. We think it is a natural assumption, but it is impossible to prove or disprove this assumption with our data set, of course, because our data set does not cover the distant region: It might turn out in the future that one needs more complicated model shape than the ellipsoid-plus-cylinder shape to successfully approximate the actual shape. The extrapolated information in this subsection should therefore be regarded as predictions based on the above stated assumption, and must be tested in the future by actual observations in the distant tail.

In fact, there already exist several reports on the distant tail radius, as stated above, even though its dependence on solar wind parameters has not yet been systematically surveyed in literature. We have found, as stated above, that our model for the nominal value of $P_{SW,\mathrm{dyn}}$, obtained by using only the dayside and near-Earth tail data, gives R_{max} which is close to the average of those reported values. This suggests that the ellipsoid-plus-cylinder shape can successfully approximate the entire shape of the actual magnetopause for the nominal value of $P_{SW,\mathrm{dyn}}$. We find no a priori reason to expect that the magnetopause is close to the ellipsoid-plus-cylinder shape only for the nominal value of $P_{SW,\mathrm{dyn}}$, and thus we think the shape could be a good approximation for any value of $P_{SW,\mathrm{dyn}}$.

Finally, as we stated at the end of section 2, $P_{SW,th}$ is an important control factor for R_{max}, because the asymptotic tail magnetopause is parallel to the solar wind and thus no dynamic pressure is applied; we did not treat $P_{SW,th}$ as a control parameter in this paper, because we were primarily interested in the near-Earth magnetopause shape, but that should be done in the future. In doing it, it should be taken into account that $P_{SW,th}$ is not independent of $P_{SW,\mathrm{dyn}}$, because both of the two include the number density of the solar wind. In fact, for our lobe data set, the correlation coefficient of the two is 0.76. We note here that the significant correlation of R_{max} and $P_{SW,\mathrm{dyn}}$ in this paper could be (at least) partly due to this correlation of $P_{SW,\mathrm{dyn}}$ and $P_{SW,th}$. Distinction of the effects of $P_{SW,\mathrm{dyn}}$ and $P_{SW,th}$ is a topic of future research. A related question to be answered in the fu-

ture is whether the total magnetic flux in the asymptotic tail is controlled by $P_{SW,\mathrm{dyn}}$ and/or $P_{SW,th}$: the total flux also affects R_{max}.

6. Summary

We have applied a simple ellipsoid plus cylinder magnetopause model, similar to many old models in literature, to both the magnetopause crossing data of *Petrinec et al.* [1991] and the magnetopause flaring angle data of *Petrinec and Russell* [1996] (PR96). We have tested two models; one of which (2-parameter model) has the focus of the ellipsoid fixed at the center of the Earth while in the other model (3-parameter model) the focus position is obtained by fitting the data. After looking at the nature of the $P_{SW,\mathrm{dyn}}$ dependence of the model through a bin-wise fitting study, we have incorporated the $P_{SW,\mathrm{dyn}}$ dependence into the models explicitly and fit the models to all available data.

As a result, we have first concluded that the 3-parameter model, or the off-center focus model, is better than the 2-parameter model, or the centered focus model, based on an objective criterion which is called AIC in statistics: It is meaningful to place the focus of the ellipsoid away from the center of the Earth. It is also notable here that AIC is useful in that it provides a general and objective way to compare any two models, if the two are applied to the same data set.

Next we have compared our model with those by *Roelof and Sibeck* [1993] (RS93) and PR96. Although our model is mathematically simple, it shows generally the same magnetopause shape as that of PR96 with a more complicated functional form. That is, the mathematical form is not the reason for the difference in the magnetopause shape between RS93 and PR96 when $P_{SW,\mathrm{dyn}}$ is extremely small or large. We suspect this difference is due to the assumed high-order dependence on $P_{SW,\mathrm{dyn}}$ of RS93's model parameters. In their model, each geometrical parameter of the ellipsoid is expressed as an exponent of a quadratic function of $\log(P_{SW,\mathrm{dyn}})$. On the other hand, in our model, most geometrical parameters (except ε) are expressed as an exponent of a linear function of $\log(P_{SW,\mathrm{dyn}})$. Our results imply that a linear function is good enough for actual observations. If a quadratic function is used, it would show large deviation from a linear pattern near and beyond the edge of the $P_{SW,\mathrm{dyn}}$ range of the data to which the model was fit.

Our model and the PR96 model generally agree as we said above, but if one looks in detail, there are some disagreements. When $P_{SW,\mathrm{dyn}}$ is extremely small, our subsolar magnetopause lies a little closer to the Earth than that of PR96, and the flaring angle of the near-Earth tail magnetopause is a little smaller than theirs (see, e.g., Figure 7a). On the other hand, when $P_{SW,\mathrm{dyn}}$ is extremely large, the near-Earth tail magnetopause of our model flares more than the PR96 model (see, e.g., Figure 9e). This difference may arise from the fact that the X dependence of the slope of PR96's model magnetopause is independent of $P_{SW,\mathrm{dyn}}$ (except for a shift in X, or in other words the X offset). In any case, this difference is limited to the near-Earth tail region; if we look at a wider region, our model and the PR96 model show good agreement, and thus their finding that their model is more (less) flaring than the RS93 model when $P_{SW,\mathrm{dyn}}$ is extremely small (large) is also the case for our model.

In this paper we have limited our analysis to the data when IMF B_Z was positive. As we mentioned in section 2, this is because we wanted to simplify this paper and concentrate on its two major points. Taking into account the IMF B_Z effect is a topic of future research.

Finally, we note that *Shue et al.* [1997a] have proposed yet another magnetopause shape model. This model makes very similar predictions to the PR96 model for high $P_{SW,\mathrm{dyn}}$ [*Shue et al.*, 1997b].

Appendix: Derivation of F

By substituting (12) into (15), we get

$$F = \frac{1}{2}\log 2\pi\sigma_r^2 + \frac{1}{N}\sum_{m=1}^{N}\frac{(r_{\mathrm{obs},m} - r_{\mathrm{model},m})^2}{2\sigma_r^2} + \frac{1}{2}\log 2\pi\sigma_\alpha^2 + \frac{1}{N}\sum_{n=1}^{N}\frac{(\alpha_{\mathrm{obs},n} - \alpha_{\mathrm{model},n})^2}{2\sigma_\alpha^2} + \frac{k}{N}. \quad \text{(A1)}$$

Then, one can calculate σ_r and σ_α which minimize F, by

$$\frac{\partial F}{\partial(\sigma_r^2)} = 0$$
$$\frac{\partial F}{\partial(\sigma_\alpha^2)} = 0,$$

solutions of which are

$$\sigma_r^2 = \frac{1}{N}\sum_{m=1}^{N}(r_{\mathrm{obs},m} - r_{\mathrm{model},m})^2 \quad \text{(A2)}$$

$$\sigma_\alpha^2 = \frac{1}{N}\sum_{n=1}^{N}(\alpha_{\mathrm{obs},n} - \alpha_{\mathrm{model},n})^2. \quad \text{(A3)}$$

Then by substituting (A2) and (A3) into (A1), we obtain (16).

Acknowledgments. This work has partly been supported by the Japanese Society for the Promotion of Science. The work at UCLA was supported by the National Science Foundation under research grant ATM 94-13081 and by the National Aeronautics and Space Administration under research grant NAGW-3948.

Michel Blanc thanks D. Sibeck and another referee for their assistance in evaluating this paper.

References

Akaike, H., A new look at the statistical model identification, *IEEE Trans. Autom. Control, AC-10*, 716–723, 1974.

Efron, B., and R. J. Tibshirani, *An Introduction to the Bootstrap*, Chapman and Hall, New York, 1993.

Fairfield, D. H., Solar wind control of magnetospheric pressure (CDAW 6), *J. Geophys. Res., 90*, 1201–1204, 1985.

Fairfield, D. H., On the structure of the distant magnetotail: ISEE 3, *J. Geophys. Res., 97*, 1403–1410, 1992.

Holzer, R. E., and J. A. Slavin, Magnetic flux transfer associated with expansions and contractions of the dayside magnetosphere, *J. Geophys. Res., 83*, 3831–3839, 1978.

Kawano, H., and T. Higuchi, The bootstrap method in space physics: error estimation for the minimum variance analysis, *Geophys. Res. Lett., 22*, 307–310, 1995.

Kessel, R. L., S.-H. Chen, J. L. Green, S. F. Fung, S. A. Boardsen, L. C. Tan, T. E. Eastman, J. D. Craven, and L. A. Frank, Evidence of high-latitude reconnecting during northward IMF: Hawkeye observations, *Geophys. Res. Lett., 23*, 583–586, 1996.

Lui, A. T. Y., Solar wind influence on magnetotail configuration and dynamics, in *Solar Wind-Magnetosphere Coupling*, edited by Y. Kamide and J. Slavin, pp. 671–690, Terra Sci., Tokyo, 1986.

Michel, F. C., and A. J. Dessler, Diffusive entry of solar flare particles into the geomagnetic tail, *J. Geophys. Res., 75*, 6061–6072, 1970.

Nakai, H., Y. Kamide, and C. T. Russell, Influences of solar wind parameters and geomagnetic activity on the tail lobe magnetic field - A statistical study, *J. Geophys. Res., 96*, 5511–5523, 1991.

Nakamura, R., S. Kokubun, T. Mukai, and T. Yamamoto, Changes in the distant tail configuration during geomagnetic storms, *J. Geophys. Res., 102*, 9587–9601, 1997.

Petrinec, S. M., and C. T. Russell, Factors which control the size of the magnetosphere, in *Solar Terrestrial Predictions IV*, vol. 2, edited by J. Hruska et al., pp. 627–635, Natl. Oceanic and Atmos. Admin. Environ. Res. Lab., Boulder, Colo., 1993.

Petrinec, S. M., and C. T. Russell, Comments on "Magnetopause shape as a bivariate function of interplanetary magnetic field B_z and solar wind dynamic pressure" by E. C. Roelof and D. G. Sibeck, *J. Geophys. Res., 100*, 1899–1901, 1995.

Petrinec, S. M., and C. T. Russell, Near-Earth magnetotail shape and size as determined from the magnetopause flaring angle, *J. Geophys. Res., 101*, 137–152, 1996.

Petrinec, S. M., P. Song, and C. T. Russell, Solar cycle variations in the size and shape of the magnetopause, *J. Geophys. Res., 96*, 7893–7896, 1991.

Press, W. H., S. A. Teukolsky, W. T. Vetterling, and B. P. Flannery, *Numerical Recipes in FORTRAN: The Art of Scientific Computing*, 2nd ed., Cambridge Univ. Press, New York, 1992.

Roelof, E. C., and D. G. Sibeck, Magnetopause shape as a bivariate function of interplanetary magnetic field B_z and solar wind dynamic pressure, *J. Geophys. Res., 98*, 21421–21450, 1993.

Roelof, E. C., and D. G. Sibeck, Reply, *J. Geophys. Res., 100*, 1903–1910, 1995.

Scurry, L., and C. T. Russell, Proxy studies of energy transfer to the magnetosphere, *J. Geophys. Res., 96*, 9541–9548, 1991.

Shue, J.-H., J. K. Chao, H. C. Fu, C. T. Russell, P. Song, K. K. Khurana, and H. J. Singer, A new functional form to study the solar wind control of the magnetopause size and shape, *J. Geophys. Res., 102*, 9497–9511, 1997a.

Shue, J.-H., P. Song, C. T. Russell, J. T. Steinberg, and J. K. Chao, Magnetopause location on January 11, 1997 event, *Eos Trans. AGU, 78(17)*, Spring Meet. Suppl., S264, 1997b.

Sibeck, D. G., G. L. Siscoe, J. A. Slavin, and R. P. Lepping, Major flattening of the distant geomagnetic tail, *J. Geophys. Res., 91*, 4223–4237, 1986.

Sibeck, D. G., R. E. Lopez, and E. C. Roelof, Solar wind control of the magnetopause shape, location, and motion, *J. Geophys. Res., 96*, 5489–5495, 1991.

Slavin, J. A., E. J. Smith, P. R. Gazis, and J. D. Mihalov, A Pioneer-Voyager study of the solar wind interaction with Saturn, *Geophys. Res. Lett., 10*, 9-12, 1983.

Slavin, J. A., E. J. Smith, D. G. Sibeck, D. N. Baker, R. D. Zwickl, and S. -I Akasofu, An ISEE 3 study of average and substorm conditions in the distant magnetotail, *J. Geophys. Res., 90*, 10875–10895, 1985.

Song, P., and C. T. Russell, Model of the formation of the low-latitude boundary layer for strongly northward interplanetary magnetic field, *J. Geophys. Res., 97*, 1411–1420, 1992.

T. Higuchi, Institute of Statistical Mathematics, 4-6-7 Minami-Azabu, Minato-ku, Tokyo 106, Japan. (higuchi@ism.ac.jp)

H. Kawano, Department of Earth and Planetary Sciences, Kyushu University 33, 6-10-1 Hakozaki, Higashi-ku, Fukuoka City, Fukuoka 812-8581, Japan. (hkawano@geo.kyushu-u.ac.jp)

S. M. Petrinec, Lockheed Martin Advance Technology Center, 3251 Hanover Street, Palo Alto, CA 94304-1187. (petrinec@lassen.spasci.com)

C. T. Russell, Institute of Geophysics and Planetary Physics, University of California, Los Angeles, CA 90095-1567. (ctrussel@igpp.ucla.edu)

(Received August 1, 1997; revised July 4, 1998;
accepted July 9, 1998.)